Langmuir

Article

pubs.acs.org/Langmuir

Temperature-Programmed Electrospray–Differential Mobility Analysis for Characterization of Ligated Nanoparticles in Complex Media

De-Hao Tsai,[†] Frank W. DelRio,[†] John M. Pettibone,[†] Pin-Ann Lin,[‡] Jiaojie Tan,[†,∥] Michael R. Zachariah,[§,∥] and Vincent A. Hackley*[,†]

[†]Materials Measurement Science Division, National Institute of Standards and Technology, Gaithersburg, Maryland 20899, United States

[‡]Center for Nanoscale Science and Technology, National Institute of Standards and Technology, Gaithersburg, Maryland 20899, United States

[§]Chemical Sciences Division, National Institute of Standards and Technology, Gaithersburg, Maryland 20899, United States

[∥]Departments of Mechanical Engineering and Chemistry, University of Maryland, College Park, Maryland 20740, United States

Supporting Information

ABSTRACT: An electrospray–differential mobility analyzer (ES-DMA) was operated with an aerosol flow-mode, temperature-programmed approach to enhance its ability to characterize the particle size distributions (PSDs) of nanoscale particles (NPs) in the presence of adsorbed and free ligands. Titanium dioxide NPs (TiO_2-NPs) stabilized by citric acid (CA) or bovine serum albumin (BSA) were utilized as representative systems. Transmission electron microscopy (TEM) and inductively coupled plasma mass spectrometry were used to provide visual information and elemental-based PSDs, respectively. Results show that the interference resulting from electrospray-dried nonvolatile salt residual nanoscale particles (S-NPs) could be effectively reduced using the thermal treatment process: PSDs were accurately measured at temperatures above 200 °C for CA-stabilized TiO_2-NPs and above 400 °C for BSA-stabilized TiO_2-NPs. Moreover, TEM confirmed the volumetric shrinkage of S-NPs due to thermal treatment and also showed that the primary structure of TiO_2-NPs was relatively stable over the temperature range studied (i.e., below 700 °C). Conversely, the shape factor for TiO_2-NPs decreased after treatment above 500 °C, possibly due to a change in the secondary (aggregate) structure. S-NPs from BSA-stabilized TiO_2-NPs exhibited higher global activation energies toward induced volumetric shrinkage than those of CA-stabilized TiO_2-NPs, suggesting that activation energy is dependent on ligand size. This prototype study demonstrates the efficacy of using ES-DMA coupled with thermal treatment for characterizing the physical state of NPs, even in a complex medium (e.g., containing plasma proteins) and in the presence of particle agglomerates induced by interaction with binding ligands.

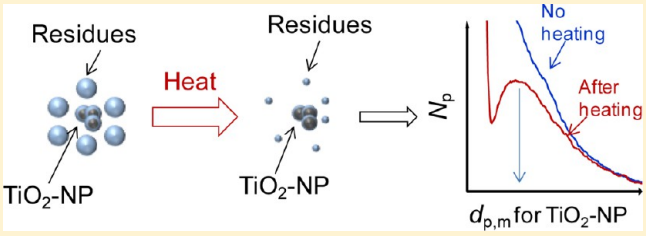

1. INTRODUCTION

The electrospray–differential mobility analysis (ES-DMA) technique has been effectively exploited as a high-resolution method to characterize the size and size distributions of engineered nanoscale particles (NPs) dispersed in aqueous media.[1−12] In the standard configuration, the suspension is introduced to the ES device and is subsequently converted into an aerosol. The aerosol containing the full spectrum of NP sizes is then fed to the DMA column where size selection is obtained based on the ion-mobility principle.[2,4,9,12,13] The narrowly size-selected aerosol stream can then be directed to a condensation particle counter (CPC) to obtain the number concentration, collected on grids for ex-situ electron microscopy analysis,[5,9,14] or coupled to an inductively coupled plasma mass spectrometer (ICP-MS) for quantitative in-situ elemental analysis.[15−19] The particle size distribution (PSD) is obtained by scanning through a predetermined range of applied voltages in the DMA. For monodisperse NPs, in addition to characterizing the native NPs, the surface packing density of functional ligands as well as the corresponding ligand molecular conformation on the NP surface[5−7] can be assessed based on the increase in the particle mobility size following conjugation and with the use of appropriate models. Furthermore, the colloidal stability of NPs in their medium, under the influence of ionic strength, or competing binding ligands present in the suspension, can be determined in situ via continuous monitoring of PSDs using the ES-DMA technique.[8−10,14,19]

Received: June 19, 2013
Revised: August 7, 2013
Published: August 12, 2013

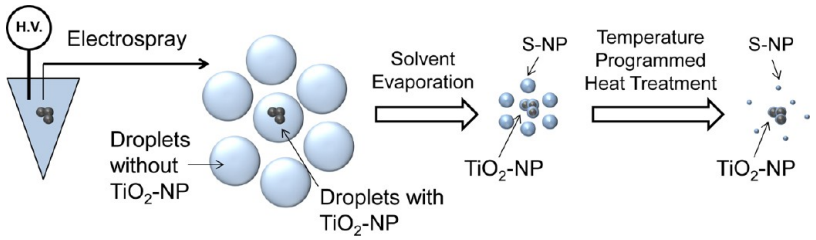

Figure 1. Conceptual model of the thermal treatment process to improve ES-DMA analysis of ligand-NP conjugates in complex media. TiO_2-NPs were the representative functional NPs.

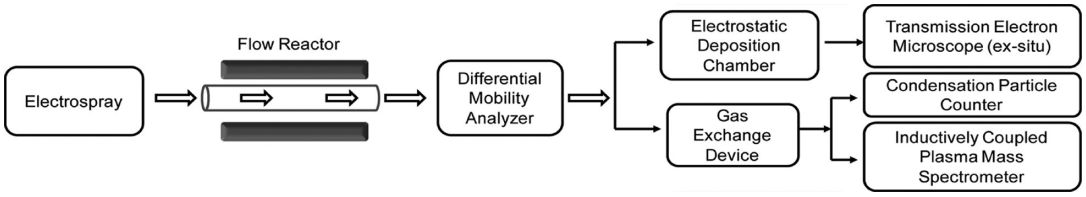

Figure 2. Schematic illustration of the measurement system used in the present study.

A substantial limitation for using ES-DMA to accurately characterize ligand-NP conjugates in relevant media is the interference from unbound ligands, or other organic and inorganic solutes, present in the solution phase.[5] As depicted in Figure 1, samples containing NPs in the solution phase are converted to monodisperse droplets by the electrospray process. As a result of the evaporation of the aerosolized droplets, the resulting aerosol contains two types of particles: (1) nonvolatile salt residue nanoparticles (S-NPs) from droplets that contain only the dissolved phase species (i.e., without the functional NPs) and (2) ligand-NP conjugates encrusted with the same nonvolatile residue from the solution phase. When the number of unbound ligands, or other compounds present in the solution phase, is sufficiently high, the particle size and PSD of the functional NPs cannot be accurately determined due to "smearing" by the dominant number intensity of S-NPs (i.e., the S-NP peak overlaps the analyte NP peak). Additionally, the residue encapsulating the target functional NPs may also bias the results of measurements toward an apparent larger size; this effect becomes significant when the native NP size is below ≈30 nm.[5,20] An example of this situation would be the analysis of NPs in cell culture medium, where the added treatment generally used for ES-DMA samples (e.g., dialysis or centrifuge-based cleaning) could be unfavorable (modify the NP physical state) or difficult to execute (difficulty increases with decreasing size).[5,9]

In the present study, we present a post-ES temperature-programmed approach to characterize ligand-NP systems using ES-DMA. Prior to size classification, all NPs aerosolized through the ES process (i.e., both the functional NPs and S-NPs) are delivered to a flow reactor (i.e., tube furnace) operated at preselected temperatures, T, as depicted in Figure 2. The principal objectives behind the approach are two-fold: (1) reduce the volume/size of S-NPs, thereby deconvoluting them from the analyte NPs of interest, and (2) remove or reduce the nonvolatile residue on functional NPs to yield native PSDs without interference. On the basis of the change in particle size and size distribution, we should be able to measure colloidal stability of NPs resulting from the interaction with binding ligands and the suspending medium. Titanium dioxide (TiO_2-NPs) was chosen as the representative functional NP because of its extensive use in industrial and consumer products[21−26] and its availability as a certified reference material.[27,28] Citric acid (CA) and bovine serum albumin (BSA) were used as stabilizing agents for the TiO_2-NP dispersions in aqueous media. As we will demonstrate, using a temperature-programmed thermal treatment, the PSDs and colloidal stability of NPs can be characterized without altering the native state of the NP suspensions via a solution phase treatment (i.e., a precleaning process is not required prior to the ES).

2. EXPERIMENTAL SECTION

2.1. Materials. Stock TiO_2-NP suspensions were prepared by adding 100.0 ± 0.1 mg of dry TiO_2 powder (Standard Reference Material 1898, Titanium Dioxide Nanomaterial, NIST)[27] to 50.0 ± 0.1 g of biological grade deionized (DI) water (resistivity >18 MΩ cm, Aqua Solutions,[29] Jasper, GA). The suspension was cooled in an ice bath and then subjected for 15 min to a probe sonicator set to an output power of approximately 50 W in pulse mode at 80% on/20% off, following a previously published protocol.[28] Subsequently, the addition of 21.4 mg of CA (Sigma-Aldrich, >99.5%, ACS reagent) was added to the solution, and the pH was adjusted to 6.4 with NaOH. The final concentration of CA was ≈2 mmol L^{-1} and was diluted with DI water on a 1:1 molar ratio prior to measurement. After adding CA and adjusting the pH, laser diffraction (LD) analysis yielded a PSD for TiO_2-NPs centered at ≈70 nm. Reagent-grade BSA (SeraCare Life Science, Milford, MA) was utilized at 150 μmol L^{-1} and directly mixed with CA-stabilized TiO_2-NPs (denoted as CA-TiO_2-NPs) on a 1:1 molar ratio to form BSA-stabilized TiO_2-NPs via displacement of CA (denoted as BSA-TiO_2-NPs). Further information on the composition and properties of SRM 1898 can be found in the literature[28] or on the certificate of analysis available from the NIST SRM Web site.[27]

2.2. Electrospray−Differential Mobility Analyzer with Temperature-Programmed Function. The ES (model 3480, TSI Inc., Shoreview, MN) generates an aerosol by using a differential pressure to move a liquid dispersion through a fused silica capillary (40 μm inner diameter tip), after which the droplets are sprayed under an electric field into a stream of dry air. The aerosolized NPs generated from the ES process are carried into the flow reactor (Lindberg Blue M Model TF55030A-1, Thermo Scientific, Madison, WI) equipped with a fused-silica tube[5] and heated to various T from 21 °C (ambient room temperature, RT) to 700 °C for a NP residence time of ≈1 s. After exiting the tube furnace, the aerosolized NPs are then delivered to the DMA (Model 3080, TSI Inc.), where the particles are classified based on their electrical mobility in an applied electric field, with a sheath flow carrying the NPs downstream. As the voltage applied to the DMA

dx.doi.org/10.1021/la402311c | Langmuir 2013, 29, 11267−11274

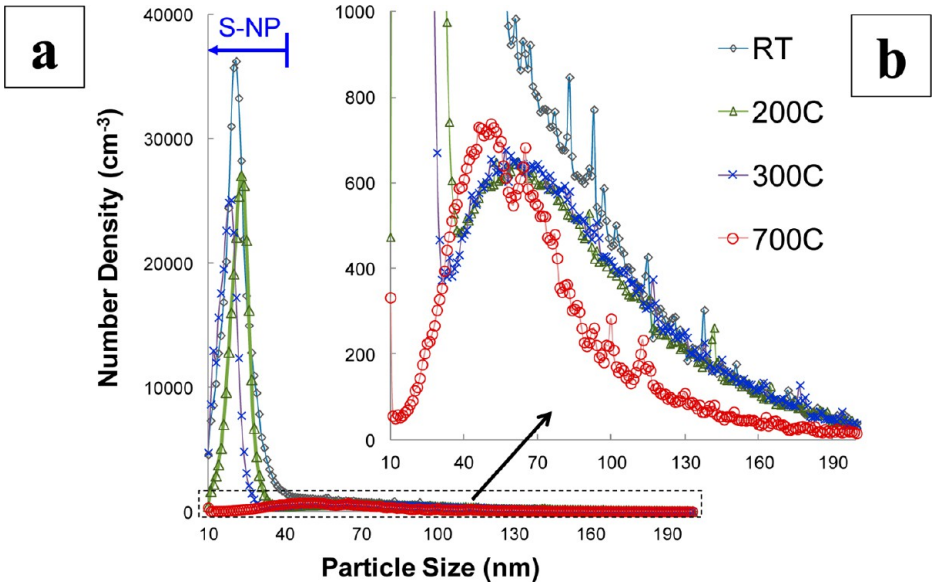

Figure 3. ES-DMA analysis of CA-stabilized TiO_2-NP suspensions. (a) PSDs as a function of temperature. (b) Magnification in *y*-axis from (a).

is varied, particles of a specific size exit the DMA[30] and are then counted by a condensation particle counter (CPC, model 3776, TSI Inc.). A Bertan power supply (205B-10R, Valhalla, NY) was used to apply voltage to the DMA in our customized system. The electric field of the DMA and data acquisition for the CPC were controlled using a customized LabView program (National Instruments, Austin, TX). The ES-DMA-CPC was used to obtain a number-based particle size distribution (i.e., number concentration of NPs in the gas phase, N_p, versus the selected mobility size of the NPs, $d_{p,m}$). The step size used in the particle size measurements was 1 nm, and the time interval between each step size was 10 s. Sheath flow rate (Q_{sh} = 5 L min^{-1}) and sample flow rate (Q_{samp}) of the DMA were controlled by a mass flow controller (MKS Instruments, Andover, MA) and a customized laminar flow element (CME, Davenport, IA), respectively. Argon was used as the sheath gas in the DMA. The resolution of the particle size measurements has been estimated previously at about 10% of the mean mobility size.[5,16,19]

2.3. Inductively Coupled Plasma Mass Spectrometer Hyphenated with ES-DMA. Inductively coupled plasma mass spectrometry (ICP-MS, 7700x, Agilent Technologies, Santa Clara, CA) was used to obtain mass-based PSDs. The ES-DMA was coupled to the ICP-MS via a gas exchange device used for resolving the incompatibility of carrier gases from ES to ICP.[16,18] Details of the hyphenated measurement system are provided in our previous publications.[16,19] The voltage applied to the DMA was increased in stepping mode, Q_{sh} was set at 10 L min^{-1}, and the $d_{p,m}$ was measured from 10 to 130 nm. Time-resolved ICP-MS acquisition mode was utilized to monitor the ^{48}Ti signal intensity as the DMA voltage was increased, allowing particles of a specific $d_{p,m}$ to exit the DMA at the selected voltage and to be atomized by the plasma and detected by the ICP-MS. The ES-DMA-ICP-MS mode was used to obtain a mass-weighted PSD. The step size used was 1 nm, and the time interval between each step size was 20 s. A relative standard uncertainty of 7% was estimated for mass distribution measurements obtained in coupled mode; this value is based on the mean standard deviation determined at each size step under repeatability conditions.[16,19]

2.4. Transmission Electron Microscopy. Transmission electron microscopy (TEM, Titan G2 60-300, FEI Inc., Hillsboro, HR) was used to identify the morphology of aerosolized NPs. TiO_2-NPs carrying a positive electrostatic charge were delivered to an electrostatic deposition chamber (Model 3089, TSI Inc.), operated at −10 kV with a sample flow rate of 1 L min^{-1}. TiO_2-NPs were deposited on a copper grid with a carbon film (SPI Supplies, West Chester, PA). Because of electrostatic repulsion, deposition-induced aggregation is negligible.[9,14] The diameter of deposited S-NPs was analyzed using ImageJ (version 1.46r, National Institute of Health). Because of the nonspherical structure of the TiO_2-NPs, TEM was only used to monitor their morphology and not for the measurement of particle diameter.

3. RESULTS AND DISCUSSION

3.1. Number-Based PSDs of CA-Stabilized TiO_2-NPs. Figure 3 shows PSDs for CA-stabilized TiO_2-NPs measured by ES-DMA-CPC at different *T*. For clarity, PSDs from four representative experimental conditions are presented in Figure 3, with additional results deferred to the Supporting Information. As shown in Figure 3a, the dominate peak at room temperature (RT, 21 °C) occurs at a $d_{p,m}$ less than 25 nm. This peak is associated with S-NPs generated by the ES process.[5,13] As the temperature increased, both the mean size and the width of the S-NP peak decreased, pointing to volumetric shrinkage of S-NPs. In fact, at *T* = 700 °C, the S-NP peak was not measurable due to limitations in instrumentation (i.e., the cutoff size for long-column DMA is 10 nm). The volumetric shrinkage is presumably due to further dehydration of S-NPs and/or thermal decomposition of organic components within the S-NPs (in this case CA).

As shown in Figure 3b, the signal corresponding to the TiO_2-NPs (typically centered at ≈70 nm as measured by LD) are indistinguishable at RT due to the high number density of S-NPs and the overlap of PSDs. At *T* > 200 °C, however, PSDs representing TiO_2-NPs (ranging from 30 to 200 nm) could be identified, even though the S-NP peak persisted up to 700 °C. The peak size of the TiO_2-NPs ($d_{p,m}$ ≈ 60 nm), and the shape of the PSD, were relatively constant for the temperature ranging from 200 to 500 °C, indicating TiO_2-NPs are thermally stable in structure (i.e., no observable changes in the primary or secondary size) under the experimental conditions (i.e., residence times and temperature) used in this study. At *T* > 600 °C (e.g., 700 °C in Figure 3), both the peak size and width of the PSD for TiO_2-NPs decreased, despite the further reduction in interference from the S-NPs. In the following section, TEM is used to determine if this decrease in signal is due to structural changes in the TiO_2-NPs during thermal treatment. Note that the TiO_2-NP dispersions used in our study were found to be relatively stable during the measure-

dx.doi.org/10.1021/la402311c | *Langmuir* 2013, 29, 11267−11274

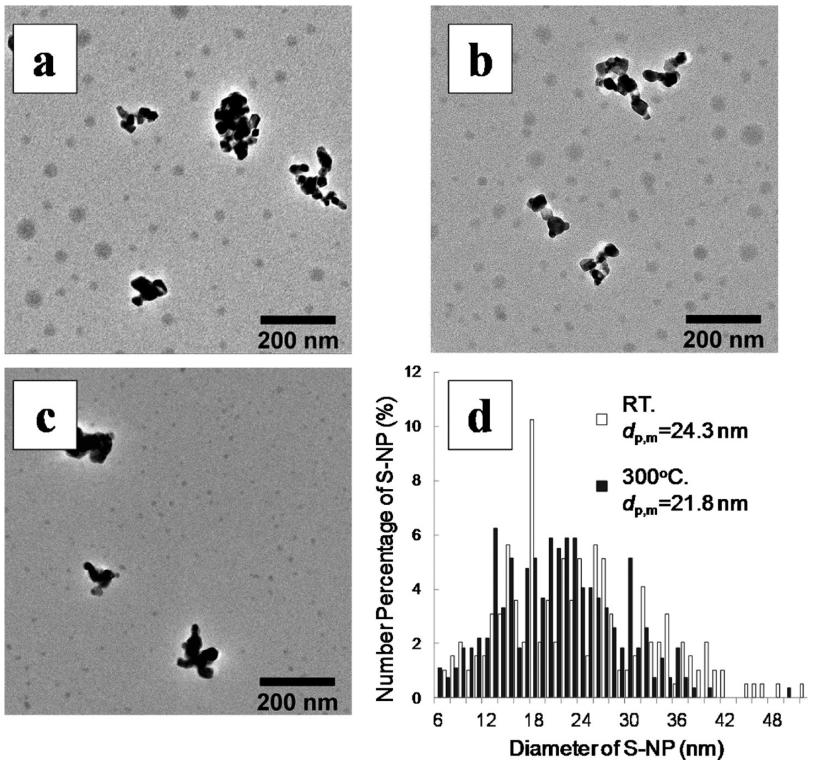

Figure 4. TEM analysis of electrosprayed CA-stabilized TiO_2-NP suspensions. (a) TEM image at RT. (b) TEM image at 300 °C. (c) TEM image at 700 °C. (d) Overlaid histograms for S-NPs at RT (unfilled) and 300 °C (filled). Number of particle counts were 195 for the RT sample and 272 for the T = 300 °C sample.

ment (e.g., absence of fast agglomeration that might alter PSDs). Because of a low number concentration of TiO_2-NPs, in comparison to the concentration of ES-generated droplets (i.e., less than one particle per 10 droplets), we assume PSDs of encapsulated TiO_2-NPs will remain unchanged following evaporation of the ES-generated droplets (i.e., agglomeration of TiO_2-NPs is unlikely).

3.2. Primary and Secondary Structure of CA-Stabilized TiO_2-NPs. Figure 4 presents TEM images of electrosprayed particles captured in situ. From the TEM images, it is clear that both TiO_2-NPs and S-NPs were homogenously distributed on the grids during the electrostatic deposition.[5,14] The larger, less frequent NPs with dark contrast are TiO_2-NPs, whereas the smaller, more ubiquitous NPs are S-NPs, as determined by the Ti trace from energy dispersive spectroscopy (details shown in Supporting Information). As temperature increased from room temperature (Figure 4a) to 300 °C (Figure 4b) to 700 °C (Figure 4c), the S-NPs significantly decreased in size and exhibited a more homogeneous PSD. Because of the difficulty associated with identifying these differences simply from the images, histograms were used to quantify the change in particle size of S-NPs. As shown in Figure 4d, the PSD of S-NPs at T = 300 °C was more narrow with a smaller average diameter (21.8 ± 7.4 nm) than that at RT (24.3 ± 9.3 nm); the difference was mainly attributed to the reduction of S-NPs with a diameter larger than 30 nm. TEM results confirmed that the inference from S-NPs can be further decreased as T increases, as observed in Figure 3. Note that the number of particles counted was 195 for the RT sample and 272 for the T = 300 °C sample. The uncertainty in average diameter was defined as one standard deviation of all data points.

TEM images were then used to examine the structure of size-resolved TiO_2-NPs at three different temperatures: RT, 300 °C, and 700 °C. Figures 5a and 5b are representative images of

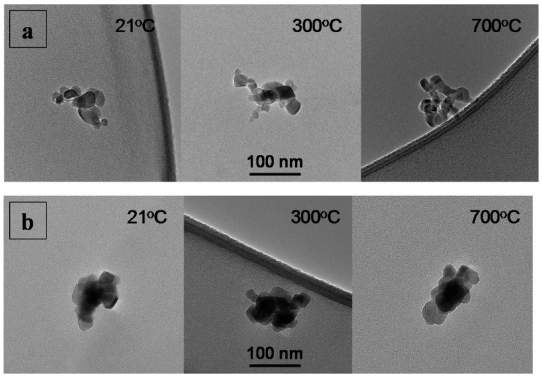

Figure 5. TEM images of size-selected CA-stabilized TiO_2-NPs at RT, 300 °C, and 700 °C: (a) $d_{p,m}$ = 53 nm; (b) $d_{p,m}$ = 83 nm.

TiO_2-NPs (additional images available in the Supporting Information). The TiO_2-NPs have a primary structure (nanoscale crystallites), with a secondary structure (aggregates of fused primary crystallites) that is random and possibly fractal in nature. The primary crystallites (anatase and rutile) range from ≈10 to 50 nm, with a volume-weighted mean size of about 24 nm.[28] Up to 700 °C, the primary structure of the TiO_2-NPs is relatively stable, as the combination of high temperature but low residence time is insufficient to induce further sintering between the primary crystallites. Figure 5 also confirms that TiO_2-NPs with a larger mobility size ($d_{p,m}$ = 83 nm) exhibit a larger (and apparently higher electron density)

dx.doi.org/10.1021/la402311c | Langmuir 2013, 29, 11267−11274

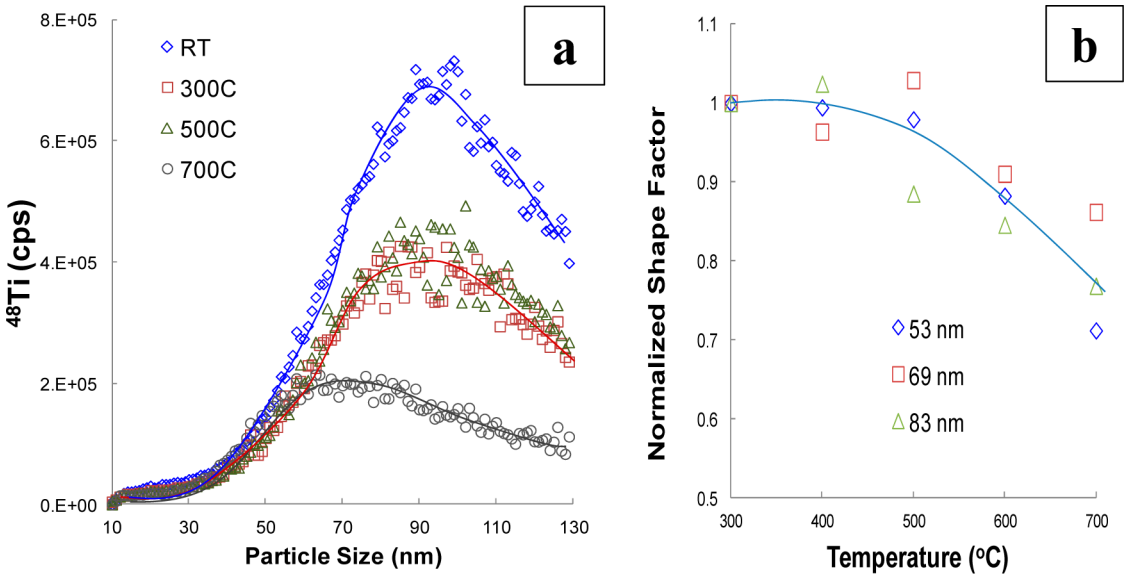

Figure 6. Analysis of relative mass and shape factor for TiO_2-NPs. (a) Elemental-based PSDs of CA-stabilized TiO_2-NP suspensions measured by ES-DMA-ICP-MS. (b) Change in normalized shape factor, $X(T)^*$, versus temperature.

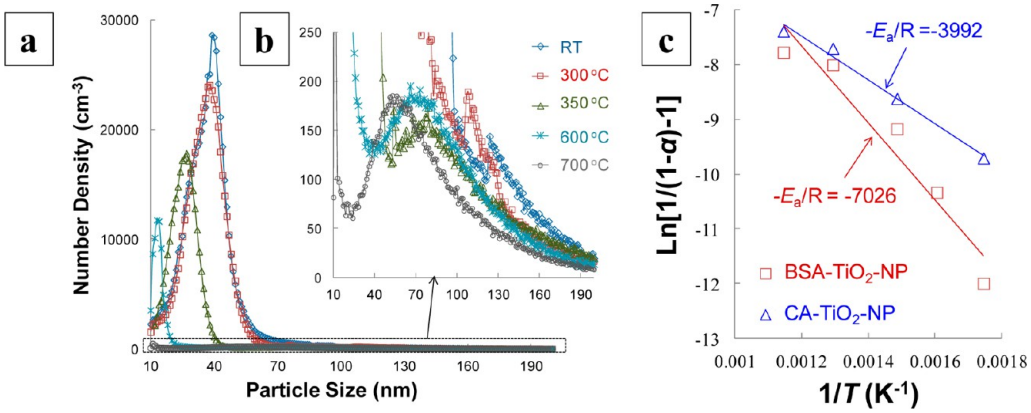

Figure 7. ES-DMA analysis of BSA-stabilized TiO_2-NP suspensions: (a) PSDs as a function of temperature; (b) *y*-axis expanded view of Figure 6a; (c) calculation of E_a using eqs 3 and 4.

secondary structure. On the other hand, because of the complexity of the secondary structure (i.e., a broad PSD of primary particles with a variable number of primary particles per TiO_2-NP), it is not possible to clearly identify thermally induced changes simply based on analysis of TEM images.

3.3. Relative Mass and Shape Factor of CA-Stabilized TiO_2-NPs. It is possible, however, to track changes in particle structure by measuring the shape factor, $X(T)$, of the TiO_2-NPs as given by

$$X(T) = d_{p,m}/\sqrt[3]{M^*} \quad (1)$$

where M^* is the relative mass of the TiO_2-NPs at a specific $d_{p,m}$. If the conformation of TiO_2-NPs became more compact due to heat treatment, we should be able to see a decrease in $X(T)$ at the same $d_{p,m}$, (i.e., high fractal dimension).[31,32] In recent work, a joint measurement approach was used to determine M^* for gold nanoparticle clusters; ICP-MS was used as a downstream detector to track the elemental counts, N_e, over a range of selected $d_{p,m}$, and the CPC was used to measure the number concentration, N_p, which together yielded $M^* = N_e/N_p$.[19] Here, a similar approach is used to determine M^*, and thus $X(T)$, for the TiO_2-NPs.

Figure 6a shows the mass-based TiO_2-NP PSDs as a function of treatment temperature. Similar to the number-based PSDs shown in Figure 3, broad PSDs ranging from 30 to 130 nm (130 nm is the upper limit of the measurement in the configuration used for this study) were observed. From room temperature to 500 °C, the mass-average mean $d_{p,m}$ was 95.3–97.6 nm (using the data shown in Figure 6a), considerably larger than the number-based peak value ($d_{p,m} \approx 60$ nm, as shown in Figure 3). The difference in the central tendency of the peak can be attributed to the difference in weighting between number- and mass-based PSDs (a factor of d^3), the nonspherical nature of these NPs, and the broad PSD.[16,30] Above room temperature, the mass-based PSDs are qualitatively similar to the PSD at room temperature. In detail, however, the central tendency of the peak decreases slightly as the temperature increases, possibly due to the partial removal of residue on the surface of the TiO_2–NPs (shell thickness of ≈0.5 nm at room temperature and 0.2 nm at 300 °C). At 700 °C, the mass-based PSD is significantly narrower, exhibiting a considerable decrease in the mass-average mean $d_{p,m}$ to 82.6 nm. Note that the decrease in peak mass intensity is mainly attributed to the thermophoresis-induced transport loss.[33]

dx.doi.org/10.1021/la402311c | *Langmuir* 2013, 29, 11267–11274

Table 1. $d_{p,m}$ Measured for CA-TiO_2-NPs and BSA-TiO_2-NPs as a Function of Temperature

	$d_{p,m}$ of S-NP (nm)						$d_{p,m}$ of TiO_2-NP (nm)					
samples	RT	300 °C	400 °C	500 °C	600 °C	700 °C	RT	300 °C	400 °C	500 °C	600 °C	700 °C
CA- TiO_2-NPs	20	18	15	12	11			60	59	58	57	51
BSA-TiO_2-NPs	39	37	19	14	13	11			70	69	69	56

Using N_p from Figure 3 and N_e from Figure 6a, $X(T)$ was calculated for representative particle sizes (52, 69, and 82 nm) with eq 1 and subsequently normalized to avoid potential variation in transport loss across different measurements using the relationship

$$X(T^*) = X(T)/X(300\ °C) \tag{2}$$

where $X(T)^*$ is the normalized value of $X(T)$ and $X(300\ °C)$ is $X(T)$ at $T = 300$ °C. As shown in Figure 6b, $X(T)^*$ is relatively constant over temperatures from 300 to 500 °C. However, at $T > 500$ °C, $X(T)^*$ decreases with increasing temperature. Thus, the results confirm that secondary structural changes occur at higher temperatures, resulting in a more compact morphology most likely due to thermally induced sintering between the primary crystallites (possibly accompanied by anatase-to-rutile phase transformation) within the nanoscale aggregates. Although it was not possible to confirm sintering based on the TEM images alone, temperature-programmed ES-DMA measurements provide greater sensitivity for monitoring such subtle morphological changes.

3.4. Activation Energy for Volumetric Shrinkage of CA and BSA S-NPs. In this section, the global activation energy for volumetric shrinkage of S-NPs, E_a, is investigated. This global activation energy represents a combination of processes involving dehydration, thermal decomposition, and/or denaturing of organic components within the S-NPs. BSA was chosen as a representative large ligand (compared to CA) due to its prominent use in biological testing and as a representative plasma protein.[7,34−37] Because of its high binding affinity through electrostatic and hydrophobic interactions,[37] it was hypothesized that BSA would preferably (relative to CA) attach to the surface of the TiO_2-NPs until surface saturation was reached. Figure 7a shows PSDs for BSA-TiO_2-NPs; the equilibrium concentration of BSA was more than 2× greater than the amount required for surface saturation.[37,38] Similar to Figure 3a, the PSDs in Figure 7a exhibit a broad peak with a strong intensity corresponding to S-NPs at room temperature. However, in this case, the S-NPs are formed by droplet induced aggregation of the relatively large BSA molecules remaining in solution,[13,39] and as a result, $d_{p,m}$ for the S-NPs in Figure 7a (peak at ≈39 nm) is larger than that in Figure 3a for CA-stabilized TiO_2-NPs. The increase in size for the S-NP peak leads to a complete overlap with the PSD corresponding to the native TiO_2-NPs in the absence of thermal treatment.

By heating to 300 °C, $d_{p,m}$ for the S-NPs decreased slightly from 39 to 37 nm, whereas the PSD for TiO_2-NPs remained unresolvable. However, $d_{p,m}$ decreased dramatically at 350 °C (to ≈27 nm) and continued to shrink with further increases in T as shown in Table 1. As a result, PSDs representing TiO_2-NPs were distinguishable and relatively unchanged for T from 350 to 600 °C, as shown in Figure 7b. However, $d_{p,m}$ for the TiO_2-NPs decreased at 700 °C as shown in Table 1, largely due to a change in the secondary structure as discussed previously. In all, the results establish that the required temperature for characterization of BSA-TiO_2-NPs is higher relative to CA-TiO_2-NPs.

The rate constant, k, for inducing the volume shrinkage of both CA and BSA S-NPs was determined using data from Figures 3 and 7, respectively, with a second-order approximation[40]

$$k = \left(\frac{1}{1-\alpha} - 1\right)/t \tag{3}$$

where t is the reaction time ($t = 1$ s in our study) and α is the volumetric change ratio defined as $\alpha = (V_{t=0} - V_t)/V_{t=0}$. V_t is the volume of the S-NPs after thermal treatment and $V_{t=0}$ is V_t without treatment. E_a was then obtained from k based on the Arrhenius equation

$$E_a = -RT_p[\ln(k) - A_1] \tag{4}$$

where A_1 is a constant, R is the gas constant, and T_p is the temperature of the S-NPs. Here we assume T_p is equal to T (the preselected tube furnace temperature), although the evaporation of water within the TiO_2-NPs could potentially depress T_p. As shown in Figure 7c, $E_a \approx 58.4$ kJ mol^{-1} for BSA S-NPs, close to the value of the unbound BSA-only sample (details shown in Supporting Information), $E_a \approx 51.9$ kJ mol^{-1}. These values are higher than the value for CA S-NPs, ≈ 33.2 kJ mol^{-1}, indicating that the addition of BSA changes E_a. More generally, the results suggest E_a for S-NPs is dependent on the size of the ligand. Therefore, the technique can be used to remove the interference from any unbound organic ligand by altering the temperature during the characterization of PSDs of functional NPs by ES-DMA. Note that the data used to calculate E_a range from $T = 300$ °C to $T = 600$ °C. Also, we note the linear fit for obtaining E_a for BSA S-NPs is less ideal in comparison to CA S-NPs, indicating multiple processes may exist that involve reactions beyond the second order used to derive the combined E_a.

The results in Figure 7 also indicate a higher temperature may be required to distinguish the PSD of ligand-bound TiO_2-NPs containing a higher mass concentration of unbound ligands. In our experiment, the mass concentration of unbound ligand in CA-TiO_2-NPs was increased by more than 2× after addition of BSA (i.e., BSA-TiO_2-NPs), resulting in an increase in particle size for S-NPs. In order to distinguish the PSD of TiO_2-NPs from the interference of S-NPs in a higher concentration of unbound ligands, it was necessary to induce further volumetric shrinkage (e.g., at least a 67% decrease in the volume of the S-NP, as shown in Figure 6a).

Without this interference, it becomes clear from Figure 7 that the $d_{p,m}$ of TiO_2-NPs coated with BSA is ≈11−12 nm larger than that for TiO_2-NPs only stabilized with CA. The increase in $d_{p,m}$ is due to a thicker corona formed on the surface of the TiO_2-NPs after interacting with BSA. At $T = 700$ °C and beyond, though, the difference in $d_{p,m}$ decreases, due to either changes in the secondary structure of the TiO_2-NPs or thermal desorption of the BSA from the surface of the TiO_2-NPs.

The method proposed in this work can be applied to different types of NP systems under a variety of ligand interaction conditions. At the appropriate temperatures, PSDs

dx.doi.org/10.1021/la402311c | Langmuir 2013, 29, 11267−11274

and the corresponding colloidal stability can be monitored without altering the solution phase environment prior to measurement. Even though it is feasible to measure the desorption process of ligands at moderate temperatures,[5,41] a major restriction of this method is its ability to measure the adsorption of ligands on NPs based on the change in physical size (i.e., some surface-bound ligands may be destroyed by heat treatment at critical conditions). In addition, the applicability of this approach is dependent on the thermal stability of the NPs, since the maximum treatment temperature (i.e., without causing conformation changes within the particles) can be quite different (e.g., 300 °C for AuNPs in comparison to 700 °C for TiO_2-NPs, based on our TP-ES-DMA results). Additional limitations may restrict the threshold particle size above which the method can be applied, a topic worthy of further investigation but beyond the scope of the present work. An alternate method to measure the $d_{p,m}$ by ES-DMA at a lower treatment temperature is to hyphenate ES-DMA with ICP-MS and perform salt residue correction calculations.

4. SUMMARY AND CONCLUSIONS

In summary, an ES-DMA was used in combination with a temperature-programmed approach to enhance the capacity to characterize ligated TiO_2-NPs. By heating the electrosprayed aerosols to a sufficient temperature, interference from the dried solution residue was effectively reduced or eliminated. The relative mass and shape factors for TiO_2-NPs were measured through the hyphenation of ES-DMA with ICP-MS. Above a critical temperature (e.g., 600 °C for TiO_2-NPs), the thermal treatment may result in a change in secondary structure (shape factor). The global activation energy to induce volumetric shrinkage of residual S-NPs is higher for BSA-TiO_2-NPs than CA-TiO_2-NPs, suggesting that the activation energy may be dependent on the size of unbound organic ligands. Taken together, the results validate a prototype method for characterizing particle size distributions of inorganic NPs using ES-DMA, even when present in a complex medium (e.g., with plasma proteins) and in the presence of particle agglomerates induced by an interaction with binding ligands. Future work will seek to improve the quantitative analysis of ES-DMA-ICP-MS by optimizing the plasma tuning and the gas exchange efficiency, in addition to measuring the absolute values of particle mass in different environmental conditions (e.g., temperature, aqueous phase composition).

■ ASSOCIATED CONTENT

Ⓢ Supporting Information

Number-based particle size distributions for CA-stabilized TiO_2-NPs as a function of temperature; TEM analysis of thermally treated CA-stabilized TiO_2-NPs; volumetric shrinkage of unbound BSA; TEM image of as-received TiO_2 powder. This material is available free of charge via the Internet at http://pubs.acs.org.

■ AUTHOR INFORMATION

Corresponding Author

*E-mail vince.hackley@nist.gov (V.A.H.).

Notes

The authors declare no competing financial interest.

■ ACKNOWLEDGMENTS

The authors thank Michael Winchester, Renu Sharma, Mingdong Li, Xiaofei Ma, and Jingyu Liu at NIST for providing some hardware components/facility used in this study, useful discussions, and review of the manuscript.

■ REFERENCES

(1) Anumolu, R.; Gustafson, J. A.; Magda, J. J.; Cappello, J.; Ghandehari, H.; Pease, L. F. Fabrication of Highly Uniform Nanoparticles from Recombinant Silk-Elastin-like Protein Polymers for Therapeutic Agent Delivery. *ACS Nano* **2011**, *5*, 5374−5382.

(2) Hogan, C. J.; Ruotolo, B. T.; Robinson, C. V.; de la Mora, J. F. Tandem Differential Mobility Analysis-Mass Spectrometry Reveals Partial Gas-Phase Collapse of the GroEL Complex. *J. Phys. Chem. B* **2011**, *115*, 3614−3621.

(3) Hogan, C. J.; de la Mora, J. F. Ion Mobility Measurements of Nondenatured 12−150 kDa Proteins and Protein Multimers by Tandem Differential Mobility Analysis-Mass Spectrometry (DMA-MS). *J. Am. Soc. Mass Spectrom.* **2011**, *22*, 158−172.

(4) Pease, L. F. Physical Analysis of Virus Particles Using Electrospray Differential Mobility Analysis. *Trends Biotechnol.* **2012**, *30*, 216−224.

(5) Tsai, D. H.; Zangmeister, R. A.; Pease, L. F., III; Tarlov, M. J.; Zachariah, M. R. Gas-Phase Ion-Mobility Characterization of SAM-Functionalized Au Nanoparticles. *Langmuir* **2008**, *24*, 8483−8490.

(6) Tsai, D. H.; Elzey, S.; DelRio, F. W.; Keene, A. M.; Tyner, K. M.; Clogston, J. D.; MacCuspie, R. I.; Guha, S.; Zachariah, M. R.; Hackley, V. A. Tumor Necrosis Factor Interaction with Gold Nanoparticles. *Nanoscale* **2012**, *4*, 3208−3217.

(7) Tsai, D. H.; DelRio, F. W.; Keene, A. M.; Tyner, K. M.; MacCuspie, R. I.; Cho, T. J.; Zachariah, M. R.; Hackley, V. A. Adsorption and Conformation of Serum Albumin Protein on Gold Nanoparticles Investigated Using Dimensional Measurements and in Situ Spectroscopic Methods. *Langmuir* **2011**, *27*, 2464−2477.

(8) Elzey, S.; Grassian, V. H. Nanoparticle Dissolution from the Particle Perspective: Insights from Particle Sizing Measurements. *Langmuir* **2010**, *26*, 12505−12508.

(9) Tsai, D. H.; Cho, T. J.; DelRio, F. W.; Taurozzi, J.; Zachariah, M. R.; Hackley, V. A. Hydrodynamic Fractionation of Finite Size Gold Nanoparticle Clusters. *J. Am. Chem. Soc.* **2011**, *133*, 8884−8887.

(10) Elzey, S.; Baltrusaitis, J.; Bian, S. W.; Grassian, V. H. Formation of Paratacamite Nanomaterials via the Conversion of Aged and Oxidized Copper Nanoparticles in Hydrochloric Acidic Media. *J. Mater. Chem.* **2011**, *21*, 3162−3169.

(11) Buesser, B.; Pratsinis, S. E. Design of Nanomaterial Synthesis by Aerosol Processes. *Annu. Rev. Chem. Biomol.* **2012**, *3*, 103−127.

(12) Attoui, M.; Paragano, M.; Cuevas, J.; de la Mora, J. F.; Tandem, D. M. A. Generation of Strictly Monomobile 1−3.5 nm Particle Standards. *Aerosol Sci. Technol.* **2013**, *47*, 499−511.

(13) Li, M.; Guha, S.; Zangmeister, R.; Tarlov, M. J.; Zachariah, M. R. Method for Determining the Absolute Number Concentration of Nanoparticles from Electrospray Sources. *Langmuir* **2011**, *27*, 14732−14739.

(14) Tsai, D. H.; Pease, L. F., III; Zangmeister, R. A.; Tarlov, M. J.; Zachariah, M. R. Aggregation Kinetics of Colloidal Particles Measured by Gas-Phase Differential Mobility Analysis. *Langmuir* **2009**, *25*, 140−146.

(15) Carazzone, C.; Raml, R.; Pergantis, S. A. Nanoelectrospray Ion Mobility Spectrometry Online with Inductively Coupled Plasma-Mass Spectrometry for Sizing Large Proteins, DNA, and Nanoparticles. *Anal. Chem.* **2008**, *80*, 5812−5818.

(16) Elzey, S.; Tsai, D. H.; Yu, L. L.; Winchester, M. R.; Kelley, M. E.; Hackley, V. A. Real-Time Size Discrimination and Elemental Analysis of Gold Nanoparticles Using ES-DMA Coupled to ICP-MS. *Anal. Bioanal. Chem.* **2013**, *405*, 2279−2288.

(17) Kapellios, E. A.; Pergantis, S. A. Size and Elemental Composition of Nanoparticles Using Ion Mobility Spectrometry

with Inductively Coupled Plasma Mass Spectrometry. *J. Anal. At. Spectrom.* **2012**, *27*, 21−24.
(18) Nishiguchi, K.; Utani, K.; Fujimori, E. Real-Time Multielement Monitoring of Airborne Particulate Matter Using ICP-MS Instrument Equipped with Gas Converter Apparatus. *J. Anal. At. Spectrom.* **2008**, *23*, 1125−1129.
(19) Tsai, D. H.; Cho, T. J.; Elzey, S. R.; Gigault, J. C.; Hackley, V. A. Quantitative Analysis of Dendron-Conjugated Cisplatin-Complexed Gold Nanoparticles Using Scanning Particle Mobility Mass Spectrometry. *Nanoscale* **2013**, *5*, 5390−5395.
(20) National Institute of Standards and Technology Report of Investigation RM8011-RM8013, 2008.
(21) Guzman, K. A. D.; Finnegan, M. P.; Banfield, J. F. Influence of Surface Potential on Aggregation and Transport of Titania Nanoparticles. *Environ. Sci. Technol.* **2006**, *40*, 7688−7693.
(22) Liao, G. Z.; Chen, S.; Quan, X.; Chen, H.; Zhang, Y. B. Photonic Crystal Coupled TiO_2/Polymer Hybrid for Efficient Photocatalysis under Visible Light Irradiation. *Environ. Sci. Technol.* **2010**, *44*, 3481−3485.
(23) Neouze, M. A.; Litschauer, M.; Puchberger, M.; Peterlik, H. Porous Titania Ionic Nanoparticle Networks. *Langmuir* **2011**, *27*, 4110−4116.
(24) Pearson, A.; Jani, H.; Kalantar-Zadeh, K.; Bhargava, S. K.; Bansal, V. Gold Nanoparticle-Decorated Keggin Ions/TiO_2 Photocatalyst for Improved Solar Light Photocatalysis. *Langmuir* **2011**, *27*, 6661−6667.
(25) Reid, D. L.; Kreitz, K. R.; Stephens, M. A.; King, J. E. S.; Nachimuthu, P.; Petersen, E. L.; Seal, S. Development of Highly Active Titania-Based Nanoparticles for Energetic Materials. *J. Phys. Chem. C* **2011**, *115*, 10412−10418.
(26) Solovitch, N.; Labille, J.; Rose, J.; Chaurand, P.; Borschneck, D.; Wiesner, M. R.; Bottero, J. Y. Concurrent Aggregation and Deposition of TiO_2 Nanoparticles in a Sandy Porous Media. *Environ. Sci. Technol.* **2010**, *44*, 4897−4902.
(27) Certificate of Analysis, SRM 1898, National Institute of Standards and Technology, http://www.nist.gov/srm, 2012.
(28) Taurozzi, J. S.; Hackley, V. A.; Wiesner, M. R. A Standardised Approach for the Dispersion of Titanium Dioxide Nanoparticles in Biological Media. *Nanotoxicology* **2013**, *5*, 389−401.
(29) The identification of any commercial product or trade name does not imply endorsement or recommendation by the National Institute of Standards and Technology.
(30) Hinds, W. C. *Aerosol Technology: Properties, Behavior, and Measurement of Airborne Particles*, 2nd ed.; John Wiley & Sons: New York, 1999.
(31) Ma, X. F.; Lall, A. A.; Aronhime, N.; Zachariah, M. R. Catalytic Decomposition of Liquid Hydrocarbons in an Aerosol Reactor: a Potential Solar Route to Hydrogen Production. *Int. J. Hydrogen Energy* **2010**, *35*, 7476−7484.
(32) Song, D. K.; Lenggoro, I. W.; Hayashi, Y.; Okuyama, K.; Kim, S. S. Changes in the Shape and Mobility of Colloidal Gold Nanorods with Electrospray and Differential Mobility Analyzer Methods. *Langmuir* **2005**, *21*, 10375−10382.
(33) Friedlander, S. K. *Smoke, Dust, and Haze: Fundamentals of Aerosol Dynamics*; Oxford University Press: New York, 2000.
(34) Jedlovszky-Hajdu, A.; Bombelli, F. B.; Monopoli, M. P.; Tombacz, E.; Dawson, K. A. Surface Coatings Shape the Protein Corona of SPIONs with Relevance to Their Application in Vivo. *Langmuir* **2012**, *28*, 14983−14991.
(35) Lacerda, S. H. D.; Park, J. J.; Meuse, C.; Pristinski, D.; Becker, M. L.; Karim, A.; Douglas, J. F. Interaction of Gold Nanoparticles with Common Human Blood Proteins. *ACS Nano* **2010**, *4*, 365−379.
(36) Lynch, I.; Salvati, A.; Dawson, K. A. Protein-Nanoparticle Interactions What Does the Cell See? *Nat. Nanotechnol.* **2009**, *4*, 546−547.
(37) Song, L. Sorption of Bovine Serum Albumin on Nano and Bulk Oxide Particles. Master Thesis, University of Massachusetts Amherst, 2009.
(38) Fukuzaki, S.; Urano, H.; Nagata, K. Adsorption of Bovine Serum Albumin onto Metal Oxide Surfaces. *J. Ferment. Bioeng.* **1996**, *81*, 163−167.
(39) Pease, L. F. Optimizing the Yield and Selectivity of High Purity Nanoparticle Clusters. *J. Nanopart. Res.* **2011**, *13*, 2157−2172.
(40) Khawam, A.; Flanagan, D. R. Solid-State Kinetic Models: Basics and Mathematical Fundamentals. *J. Phys. Chem. B* **2006**, *110*, 17315−17328.
(41) Nishida, N.; Hara, M.; Sasabe, H.; Knoll, W. Thermal Desorption Spectroscopy of Alkanethiol Self-Assembled Monolayer on Au(111). *Jpn. J. Appl. Phys., Part 1* **1996**, *35*, 5866−5872.